catalysts

MDPI

Article

Vertically Ti_3CN@NiFe LDH Nanoflakes as Self-Standing Catalysts for Enhanced Oxygen Evolution Reaction

Lei He [1,2], Qing Tang [2,3], Qi Fan [2,4], Haizheng Zhuang [2,5], Shengchao Wang [2,4], Yifan Pang [6] and Kun Liang [2,5,*]

1 School of Materials Science and Chemical Engineering, Ningbo University, Ningbo 315211, China; helei@nimte.ac.cn
2 Zhejiang Key Laboratory of Data-Driven High-Safety Energy Materials and Applications, Ningbo Key Laboratory of Special Energy Materials and Chemistry, Ningbo Institute of Materials Technology and Engineering, Chinese Academy of Sciences, Ningbo 315201, China
3 Nano Science and Technology Institute, University of Science and Technology of China, Suzhou 215123, China
4 University of Chinese Academy of Sciences, 19 A Yuquan Rd., Shijingshan District, Beijing 100049, China
5 Qianwan Institute of CNITECH, Ningbo 315336, China
6 Department of Materials Science and Engineering, The Ohio State University, Columbus, OH 43210, USA
* Correspondence: kliang@nimte.ac.cn

Abstract: Hydrogen production from water electrolysis is gaining interest as a source of renewable energy storage due to its high efficiency and low environmental impact. However, the slow kinetics of the oxygen evolution reaction (OER) limits the overall efficiency of electrolyzer systems. This study presents the synthesis and characterization of a novel electrocatalyst with a vertical structure, composed of Ti_3CN MXene-modified NiFe-layered double hydroxides (LDHs) supported on nickel foam (NF) for efficient OER applications. The 1.0-LDH/3MXNF catalyst exhibits excellent electrocatalytic activity, achieving a low overpotential of 247 mV at a current density of 100 mA cm^{-2} and a favorable Tafel slope of 67.7 mV/dec. This can be attributed to the transfer of excess electrons from Ti_3CN MXene to NiFe-LDH, which reduces the oxidation states of Ni and Fe, resulting in a strong interfacial coupling between Ti_3CN MXene and NiFe-LDHs. Additionally, the electrode exhibited exceptional stability, maintaining constant performance with minimal potential degradation over prolonged operation. These findings underscore the potential of hybrid LDH-MXene systems as advanced electrocatalysts for renewable energy applications, paving the way for further innovations in energy conversion technologies.

Keywords: Ti_3CN-MXene; NiFe-LDH; collaborative interface; vertical structure; oxygen evolution reaction

check for updates

Citation: He, L.; Tang, Q.; Fan, Q.; Zhuang, H.; Wang, S.; Pang, Y.; Liang, K. Vertically Ti_3CN@NiFe LDH Nanoflakes as Self-Standing Catalysts for Enhanced Oxygen Evolution Reaction. *Catalysts* **2024**, *14*, 708. https://doi.org/10.3390/catal14100708

Academic Editor: Carlo Santoro

Received: 1 September 2024
Revised: 26 September 2024
Accepted: 29 September 2024
Published: 10 October 2024

1. Introduction

With escalating global concern over environmental pollution and energy consumption, there is an urgent need to develop clean and environmentally friendly energy storage and conversion technologies [1–4]. Electrochemical water decomposition (EWD) technology encompasses two half-reactions: a hydrogen evolution reaction (HER) and oxygen evolution reaction (OER), which are critical for grid-scale energy storage [5]. In alkaline media, the OER involves a complex and slow four-electron transfer process that significantly impacts the efficiency of the overall water electrolysis unit [6]. However, many materials used for this purpose consist of precious metals, rendering them unsuitable for large-scale applications due to their high cost and poor durability [7–9].

In recent years, substantial advancements have been made in the development of non-precious metal-based OER catalysts [10–15]. Among these, layered bimetallic hydroxides (LDHs), such as NiFe-LDHs [16], have demonstrated excellent OER performance in alkaline electrolytes. The coexistence of Ni^{2+} and Fe^{3+} in NiFe-LDHs, along with their synergistic effects, marks them as highly promising materials for energy conversion and

storage. Moreover, the redistribution of electron density through partial charge transfer can facilitate the oxidation of Ni^{2+}, thereby enhancing OER catalytic activity [17]. However, the OER activity of LDHs is limited by its inherent low conductivity and small surface area, which result from prone agglomeration. Nanostructures can be stabilized by constructing heterostructures with conductive substrates and LDHs [18]. Nevertheless, achieving strong interfacial synergy typically necessitates surface treatments to introduce functional groups, which can compromise the structural integrity and conductivity of the substrate material.

Two-dimensional layered materials, specifically MXene, have received considerable attention in the field of energy storage and conversion [19–26]. The general formula of MXene is $M_{n+1}X_nT_x$, where M represents a pre-transition metal element; A corresponds to the main group elements, primarily from group IIIA to VIA; X is the carbon and/or nitrogen elements; T_x denotes surface termination groups such as -OH, -O, -F, -Cl, etc.; and n can range from 1 to 4 [27–30]. To further improve the electrochemical performance of MXene, simple heteroatom doping (e.g., nitrogen) is an effective strategy [31]. Theoretically, nitrogen has fewer vacant electron orbitals than carbon and exhibits better catalytic activity [32]. For instance, Shi and Liu [33] successfully employed nitrogen to replace carbon in the lattice structure of $Ti_3C_2T_x$, resulting in increased layer spacing. Moreover, nitrogen doping modifies the electron density of Ti^{3+} by filling incomplete orbitals, which lower the energy of the valence electron system. Among various MXene materials, Ti_3CNT_x, where nitrogen replaces half of the carbon, stands out. Due to its higher electronegativity compared to carbon, the Ti-N bond is stronger than the Ti-C bond, enabling the nitrogen side to adsorb metal cations more effectively [34,35]. This characteristic facilitates strong interfacial coupling between LDH and MXene.

In this study, we employed a one-step hydrothermal method to construct a self-standing electrocatalytic electrode with a multilayer structure, leveraging the properties of Ti_3CN. A three-dimensional framework was built using Ti_3CN-modified porous nickel foam (NF), which was further interfacially coupled with NiFe-LDH nanosheets, resulting in an electrode designated as LDH/MXNF. The findings reveal a strong electrostatic interaction between the interfaces of Ti_3CN and NiFe-LDHs, enhancing the charge transfer between LDHs and MXNF. Consequently, the as-prepared LDH/MXNF self-standing electrode exhibits excellent OER performance, rapid catalytic reaction kinetics, and good stability.

2. Results and Discussion

2.1. Catalyst Synthesis and Structure Characterization

The LDH/MXNF catalyst was synthesized following the route illustrated in Figure 1. Step I: Initially, m-Ti_3CN was produced by etching off the Al layer from Ti_3AlCN using HF. This was followed by intercalation in the TMAOH solution to yield f-Ti_3CN, which was obtained through ultrasonication in deaerated water. The etching of the bulk MAX material effectively produced m-Ti_3CN (Figure S1), which showed no MAX characteristic peak at 39° (Figure S2). This result confirms the successful removal of Al layers. After exfoliation, the (002) peak of f-Ti_3CN shifted to a smaller angle (2θ = 6.0°) compared to m-Ti_3CN, indicating the successful formation of few-layered MXenes. Due to electrostatic interactions, the negatively charged f-Ti_3CN MXene coated the acid-treated porous NF surface, resulting in a uniform MXene layer wrapping around the NF surface (Figure S4). However, the MXene layer of 5MXNF exhibited cracking, likely due to its thicker structure compared to 3MXNF. Step II: In the next stage, NiFe-LDH nanosheets were grown in situ on the 3D MXNF framework by the straightforward hydrothermal synthesis method. In general, urea is highly soluble in water and its prolonged hydrolysis produces CO_3^{2-} and OH^- [36].

$$CO(NH_2)_2 + H_2O \rightarrow 2NH_3 + CO_2$$
$$NH_3 \cdot H_2O \rightarrow NH_4^+ + OH^-$$
$$CO_2 + H_2O \rightarrow CO_3^{2-} + 2H^+$$

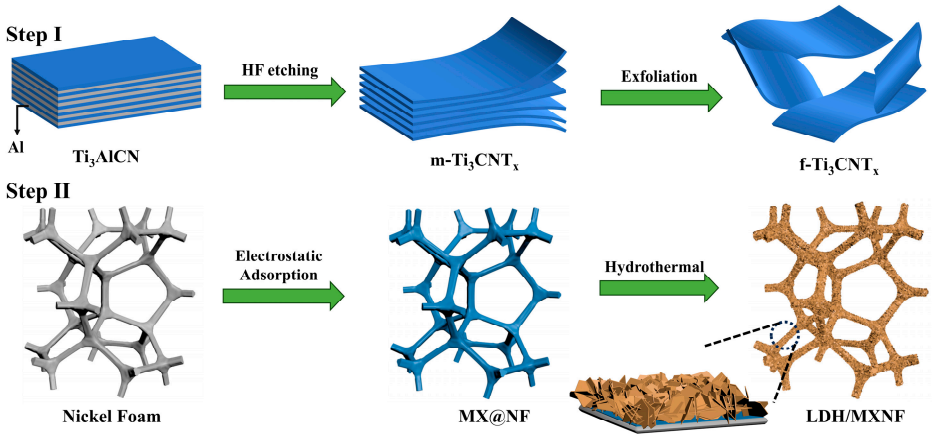

Figure 1. Schematic synthetic route of LDH/MXNF self-standing electrode.

The MXene surface, obtained through wet chemical etching and intercalation with organic bases, is characterized by negatively charged oxygen-containing functional groups. These groups can electrostatically adsorb metal cations, facilitating the precipitation and aggregation of Ni^{2+} and Fe^{3+} on the surface of the MXene-modified nickel foam. As the hydrothermal reaction proceeded, the hydrolysis of urea intensified, leading to an increased concentration of OH^- in the solution. This increase facilitated the crystallization of NiFe ions, gradually forming NiFe-LDH nanosheets.

The XRD patterns shown in Figures 2a and S3a indicate that the NiFe-LDH/NF, NiFe-LDH/MXNF, and NiFe-LDH/MCNF samples exhibit prominent diffraction peaks corresponding to Ni monomers at 44.7°, 52.1°, and 76.6°. The MXene signal is absent, likely due to the overwhelming intensity of NF and NiFe-LDH peaks, which obscures the MXene diffraction patterns. For the 1.0-LDH/3MXNF sample, the observed diffraction peaks at 11.7°, 23.2°, 34.6°, 39.0°, 46.1°, 59.9°, and 61.2° correspond to the (003), (006), (012), (015), (018), (110), and (113) lattices planes of NiFe-LDH, respectively [37]. In contrast, the intensities and crystallinities of the 0.5-LDH/3MXNF and 0.5-LDH/5MXNF samples are weaker due to the influence of NF and a lower concentration of metal cations used in their preparation. The Fourier transform infrared spectroscopy with attenuated total reflection spectra (FTIR-ATR) in Figures 2b and S3b highlight absorption peaks around 3400 cm^{-1} and 1636 cm^{-1}, which are attributed to the stretching vibration of hydrogen-bonded hydroxyl groups and the bending vibration of water molecules, respectively [38]. In addition, the absorption peak at 1350 cm^{-1} represents the C-O stretching vibration of the interlayer CO_3^{2-} [39]. The absorption peak at 2179 cm^{-1} corresponds to C-O stretching [40], consistent with the layer spacing of 7.5 Å represented by the (003) peak at 11.7° in XRD results. This suggests that the CO_3^{2-} ions generated hydrothermally from urea during synthesis act as intercalation anions, balancing the positive charge carried by the layered hydroxides. An additional absorption peak at 2185 cm^{-1} further supports the presence of CO_3^{2-} ions. Moreover, the spectral band at 640 cm^{-1} indicates the successful preparation of NiFe-LDH, attributed to the M-O vibrations in the hydroxide layers [38].

The EDS mapping of the 1.0-LDH/3MXNF sample in Figure S5 demonstrates a uniform distribution of Fe, Ti, N, and Ni across the nickel foam substrate. This uniformity suggests the successful integration of the LDH material onto the MXNF framework. The morphology and structure of NiFe-LDH nanosheets on MXNF can be effectively tuned by varying the concentrations of Ni^{2+} and Fe^{3+} ions, as well as the amount of MXene modification (Figure 2c–e). Notably, for the LDH/3MXNF self-standing electrode, the average thicknesses of the NiFe-LDH nanosheets were measured to be 16.42 nm, 27.51 nm, and 47.97 nm for metal cation additions of 0.5 mmol, 1.0 mmol, and 2.0 mmol, respectively (Figure 2f–h). The nanosheets formed on the MXNF surface exhibited a staggered and disordered arrangement, a result of the varying crystallization directions of nuclei originating from the initial aggregation of Ni^{2+} and Fe^{3+}. This unique morphology enhances

the availability of active sites and facilitates OER kinetics. Moreover, MXene serves as an interfacial bridge between NiFe-LDH and NF, improving the electron transfer ability across the electrode interface. High-resolution SEM images (Figures S6 and S7) reveal that excessive MXene modification and elevated metal ion concentrations during hydrothermal reactions can lead to cracks in the in situ grown LDH, resulting from the accumulation of internal stresses. The TEM characterization revealed that NiFe-LDH nanosheets were uniformly and densely interlaced, forming stable 3D structures on the Ti_3CN MXene surface (Figure 2i). This configuration is expected to enhance catalytic efficiency and stability for OER applications.

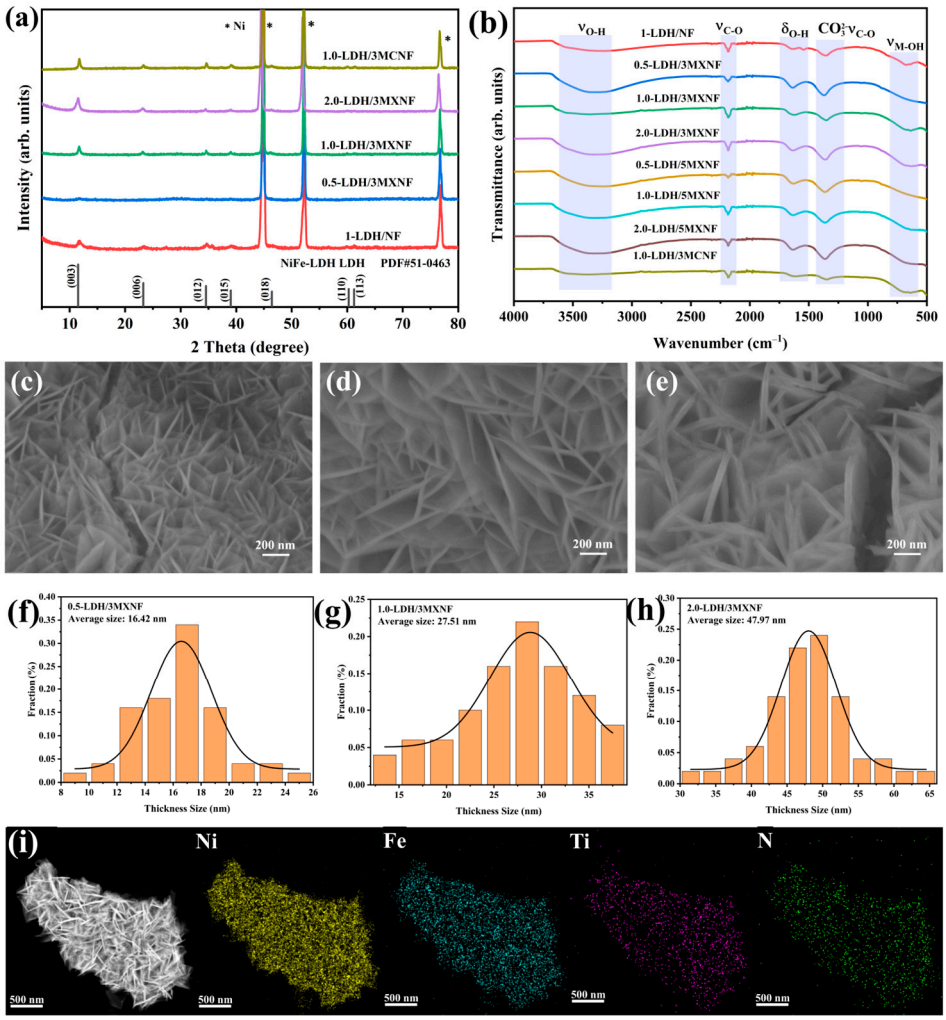

Figure 2. (**a**) XRD patterns; (**b**) ATR-FTIR spectrum of different samples; (**c**–**e**) SEM and (**f**–**h**) statistics on the thickness distributions of LDH/3MXNF; and (**i**) TEM image of 1.0-LDH/3MXNF and the corresponding EDS element mapping of Ni, Fe, Ti, and N.

X-ray photoelectron spectroscopy (XPS) was used to analyze the chemical composition and oxidation states of elements present in the 1.0-LDH/3MXNF and 1.0- LDH/NF. To minimize potential interference from the nickel foam substrate, the sample was ultrasonically stripped from the substrate prior to characterization. All peak positions were calibrated based on the C 1s peak at 284.8 eV. The XPS spectrum analysis (Figure S8) confirms the coexistence of Ni, Fe, Ti, N, O, and C elements in the 1.0-LDH/3MXNF sample, implying effective interfacial coupling between NiFe-LDH and Ti_3CN. This finding is consistent with observations from the SEM and TEM-EDS mapping images. In the Ni 2p spectrum (Figure 3a), two characteristic peaks were identified at 856.14 eV and 873.77 eV, which were attributed to the spin-orbit doublets of Ni $2p_{3/2}$ and $2p_{1/2}$ of Ni^{2+}, respectively, ac-

companied by accompanying satellite peaks (labeled as sat.) [37]. The Fe 2p spectrum (Figure 3b) displayed peaks at 711.39 eV and 724.59 eV, associated with Fe $2p_{3/2}$ and Fe $2p_{1/2}$, confirming the presence of iron primarily in the Fe^{3+} oxidation state [38]. Additionally, a satellite peak along with a pre-peak peak at 705.9 eV reinforces the identification of Fe^{3+} in the catalyst [41,42]. Notably, the binding energies of the Ni 2p and Fe 2p peaks for the NiFe-LDH/Ti_3CN composite shifted lower by 0.2–0.6 eV compared to the 1.0-LDH/NF sample. This shift suggests an increase in the electron density on the surface due to the presence of Ti_3CN, which likely facilitates electron transfer to the nickel and iron ions in the LDH. Consequently, this phenomenon indicates a strong chemical interaction between MXene and NiFe-LDH, whereby Ti_3CN effectively modulates the surface electron density and reduces the oxidation states of Fe^{3+} and Ni^{2+}.

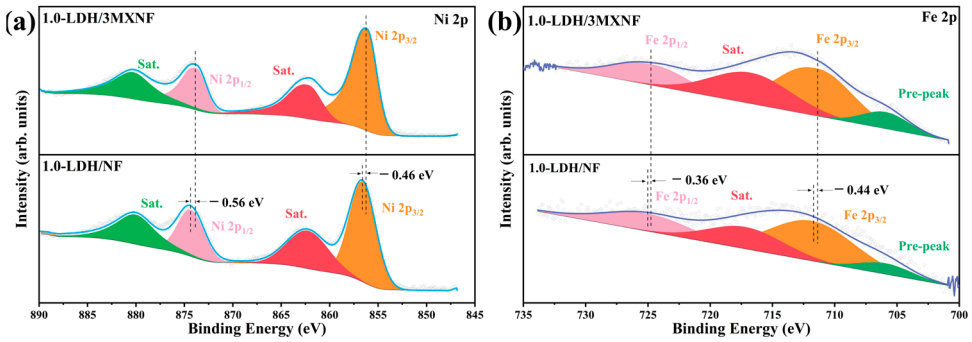

Figure 3. (**a**) Ni 2p XPS spectra of 1.0-LDH/NF and 1.0-LDH/3MXNF; (**b**) Fe 2p XPS spectra of 1.0-LDH/NF and 1.0-LDH/3MXNF.

2.2. Electrocatalytic Performance for OER

A The LDH/MXNF self-standing electrode was directly used as an electrocatalytic electrode for the OER to eliminate the influence of the binder on the active site. The catalytic performance was evaluated using a standard three-electrode setup with 1.0 M KOH as the electrolyte. The reference electrode was calibrated in 1.0 M KOH against a reversible hydrogen electrode, and subsequent potential conversions were performed using the calibration potentials (Figure S9). To further investigate the effects of MXene-modified NF and the modulation of metal cation concentration on the electrochemical performance of the monolithic electrodes, comparisons were made with samples 1.0-LDH/NF and 1.0-LDH/3MCNF, both tested under identical conditions. The LSV compensated by iR losses was tested at a low scan rate of 5 mV/s to minimize the capacitive background, allowing for a more accurate assessment of OER performance. Sample 1.0-LDH/3MXNF (Figure 4a), which utilized 1 mmol of metal ions and NF modified by a 3 mg/mL MXene dispersion, exhibited a reduced overpotential of 247 mV at a current density of 100 mA cm^{-2}. This represented a more favorable performance relative to other variations in metal ion concentrations and MXene loadings, underscoring the effective catalytic activity of the LDH/MXNF catalyst under these regulated conditions (Figure S11). Additionally, the unique 3D porous structure of NF facilitated higher current densities, with the LSV curve for 1.0-LDH/3MXNF displaying smoother characteristics at elevated current densities compared to other samples. This smoothness indicates that gas bubbles are released from the electrode surface more rapidly, enhancing kinetics related to electrolyte penetration, ionic transport, and the discharge of gaseous products during electrochemical reactions. Notably, MXene alone exhibited negligible OER catalytic performance (Figure S12), indicating that NiFe-LDH serves as the primary active site within the self-standing electrode. In this setup, MXene primarily serves as a coupling agent at the interfaces between the LDH and NF, facilitating electron transfer. However, the overall catalytic activity decreased with a higher MXene content, likely due to an increased tendency for warping and detachment following hydrothermal treatment. This adversely impacts the interfacial coupling between NiFe-LDH and NF. On the contrary, an appropriate amount of MXene can promote the effective coating of NF,

maintaining this effect even after the growth of NiFe-LDH on the MXene surface. The Tafel slope analysis (Figure 4b) for the 1.0-LDH/3MXNF catalyst further highlighted its superior kinetic reaction rates compared to other conditions, yielding a Tafel slope of 67.7 mV/dec. This low Tafel slope indicates that the rate-determining step is likely associated with the latter stages of the multi-electron transfer reaction, a characteristic of high-performance catalysts. In comparison to 1.0-LDH/NF (318 mV at 100 mA cm^{-2} and 148.1 mV/dec) and 1.0-LDH/3MCNF (270 mV at 100 mA cm^{-2} and 89.5 mV/dec), the Ti_3CN MXene-modified self-standing electrode demonstrated improved catalytic effects over electrodes featuring $Ti_3C_2T_x$ MXene or lacking MXene modification (Figure 4g). These findings suggest that both the metal cation concentration and the extent of MXene modification significantly influence the availability of active sites and electron transport within this hybrid structure, aiding in the enhanced energy efficiency of the monolithic electrode.

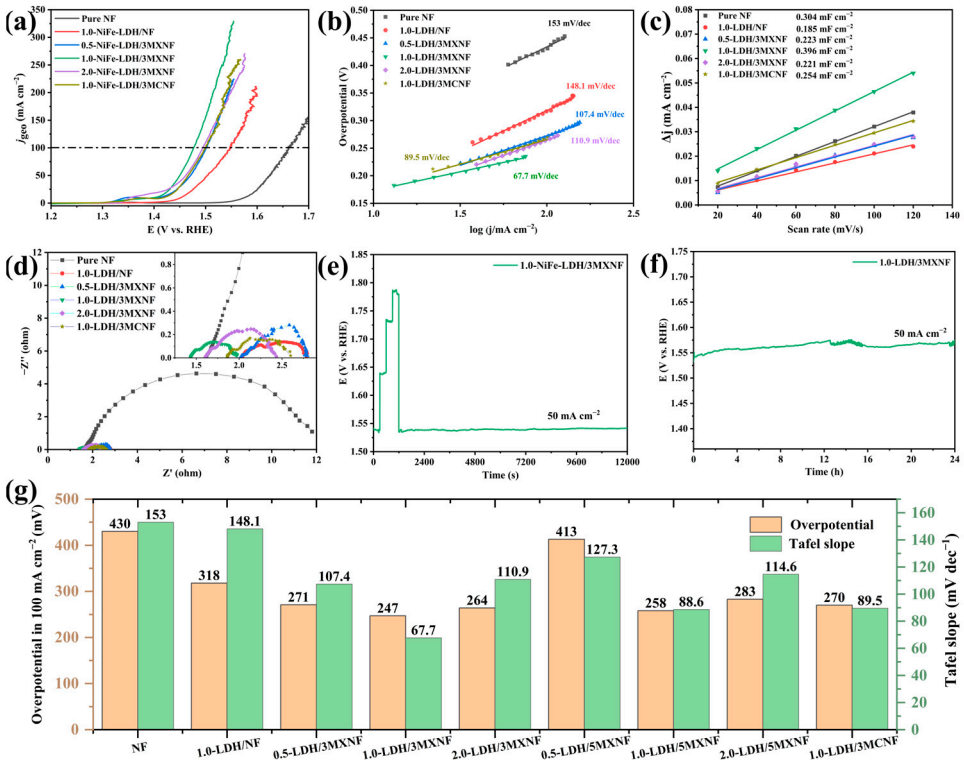

Figure 4. The OER performance of the electrocatalysts in 1.0 M KOH. (**a**) LSV curves, (**b**) Tafel plots, (**c**) the C_{dl}, (**d**) EIS patterns at 1.53 V vs. RHE, (**e**) multi-step chronopotentiometric curves, (**f**) long-term chronopotentiometric response at 50 mA cm^{-2}, (**g**) the overpotential at 100 mA cm^{-2}, and Tafel slope of (**g**) the overpotential at 100 mA cm^{-2} and Tafel slope of diagram of the as-prepared samples.

The electrochemical double-layer capacitance (C_{dl}) of the catalysts was evaluated in the non-Faradaic region using cyclic voltammetry (CV) (Figures 4c and S10). The results indicated that the vertically self-standing electrodes exhibited similar ECSAs, a finding attributed to the shared use of nickel foam as the monolithic substrate. Notably, the C_{dl} values for NF-based monolithic electrodes, such as 1.0-LDH/3MXNF (0.396 mF cm^{-2}) and 1.0-LDH/NF (0.185 mF cm^{-2}), were improved by over tenfold compared to the LDH/MXene powder catalyst (see Figure S9). The charge transfer resistance (R_{ct}) is a critical parameter related to electrode kinetics, with lower R_{ct} values indicating faster electron transfer rates. The electrochemical impedance spectroscopy (EIS) pattern presented in Figure 4d reveals that the 1.0-LDH/3MXNF sample possesses the smallest semicircle radius, corresponding to the lowest charge transfer resistance (R_{ct} = 0.51 Ω). This reduction suggests that the electron transfer kinetics are significantly faster for this sample compared

to 1.0-LDH/NF (R_{ct} = 0.82 Ω) and LDH/MXene powders (R_{ct} = 38.1 Ω). Consequently, the 1.0-LDH/3MXNF electrode substantially reduces the potential barrier for current flow through the catalyst, thereby enhancing the OER efficiency and exhibiting optimal catalytic activity. To further assess the dynamic performance of the 1.0-LDH/3MXNF electrode, a multi-step constant-current test was conducted (Figure 4e). The current density was incrementally increased from 50 mA cm^{-2} to 200 mA cm^{-2}, increasing by 50 mA cm^{-2} per step, before returning to 50 mA cm^{-2}. The electrode maintained a constant current at each step for 300 s, demonstrating rapid response times without significant fluctuations. Upon returning to 50 mA cm^{-2}, the current could be sustained for over 10,000 s without notable degradation, indicating robust electrochemical stability and mechanical integrity even under high current density conditions. Furthermore, in a long-term chronopotential (CP) stability test (Figure 4f) conducted at a constant current density of 50 mA cm^{-2}, the performance of the 1.0-LDH/3MXNF electrode remained stable over a 24 h period, with no significant increase in potential observed. This outcome underscores the excellent cycling stability and resilience of the electrode in demanding electrochemical environments. Finally, when compared to other documented OER catalysts (Table 1), the demonstrated performance of the 1.0-LDH/3MXNF catalyst remains competitive.

Table 1. OER catalysts in 1.0 M KOH that have been reported in recent years.

Catalyst	j_{geo} (mA cm^{-2})	η (mV)	Tafel Slope (mV dec^{-1})	Ref.
1.0-LDH/3MXNF	100	247	67.7	This Work
NiFe-LDH/NF	50	306	143.1	[43]
NiFeAu-LDH/NF	100	267	58	[44]
MXene/TiO_2/NiFeCo-LDH	10	320	98.4	[45]
NiCo-LDH/MXene/NF	100	257.4	68	[46]
Mo-Ni_2P@NiFe LDH/NF	40	269	44	[47]
NiCoFe-LDH/NF	50	233	29.39	[48]
CoFeV-LDH/NF	100	330	57	[49]
$Fe_{0.05}$CoNi-LDH/NF	10	212	48	[50]
$CoSnO_3$@MX/NF	100	321	101	[51]
FeCoNi-P/NF	10	239	55.87	[52]
Ni-FeOOH/NF	100	277	52	[53]
NCP-MX/NF	50	303	69.5	[54]
NiFe-LDH/rGO@NF	50	277	59.9	[55]
Cr-FeNi LDH/MXene	10	232	54.4	[2]
LDH/H-$Ti_3C_2T_x$	100	364	47	[56]
CoNi-LDH/MXene@$NiMoO_4$/NF	100	220	84.2	[57]
S,P-CoFeLDH/MXene	10	305	39	[58]
NiFe-LDH/Ti_3C_2	10	334	55	[59]

3. Materials and Methods

3.1. Chemicals

Ti_3AlCN (99% purity, 300 mesh, Laizhou KaiXi Ceramic Materials Co., Ltd., Laizhou, China), 49 wt% hydrofluoric acid (HF, Aladdin, Paris, France), 25 wt% tetramethylammonium hydroxide (TMAOH, Aladdin), iron (III) nitrate nonahydrate ($Fe(NO_3)_3{\cdot}9H_2O$, Aladdin), nickel (II) nitrate hexahydrate ($Ni(NO_3)_2{\cdot}6H_2O$, Aladdin), urea (Aladdin), ammonium fluoride (NH_4F, Aladdin), L-ascorbic acid (LAA), and potassium hydroxide (KOH, 99.99%, Aladdin). Nickel foam was purchased from Suzhou Kesheng metal materials Co., Ltd. (Suzhou, China).

All chemicals were used as received, without further purification.

3.2. Synthesis of Few-Layered Ti_3CN MXene

The few-layered Ti_3CN (f-Ti_3CN) MXene nanosheets were synthesized based on a previous report [60]. In brief, 1 g of Ti_3AICN (300 mesh) was slowly added to 10 mL of 30 wt% HF and allowed to react at room temperature for 18 h. After that, the mixture was

washed with deoxygenated water until neutral, centrifuged at 5000 rpm for 5 min each time, and finally filtered to obtain multilayered Ti_3CN (m-Ti_3CN), which was stored in a vacuum dryer overnight. The deoxygenated water was prepared by purging deionized water (DI water) with argon gas for 1 h.

Subsequently, 0.5 g of m-Ti_3CN was intercalated in 10 mL of 1 M TMAOH for 24 h. The resulting dispersion was washed with deoxygenated water until the pH reach approximately 9. During the washing process, care was taken to ensure no shaking, with each centrifugation conducted at 3500 rpm for 5 min. The f-Ti_3CN dispersion was subsequently obtained by cold bath sonication for 1 h, followed by centrifugation at 5000 rpm for 30 min.

3.3. Synthesis of LDH/MXNF

The nickel foam was thoroughly washed with acetone, 3 M HCl, and deionized water to remove any organic residues and oxide layers on the surface. A 3 × 3 cm^2 piece of NF was impregnated in 3 or 5 mg/mL of f-Ti_3CN dispersion, left to stand for 30 min, and then sonicated for an additional 30 min. The NF modified by MXene was vacuum-dried at 60 °C for 4 h, and these samples were designated as 3MXNF and 5MXNF, respectively. Next, a specific amount of $Fe(NO_3)_3 \cdot 9H_2O$ and $Ni(NO_3)_2 \cdot 6H_2O$, 1.5 g of urea, 10 mg of LAA, and 50 mg of NH_4F were dissolved in 30 mL of DI water and sonicated for 30 min. The resulting solution was then combined with the MXNF and transferred to a 50 mL Teflon-lined stainless-steel autoclave. This assembly was placed in an autoclave and heated in an air blast drying box at 120 °C for 6 h, followed by natura cooling to room temperature. The samples were then ultrasonically washed with deionized water and ethanol several times and dried under vacuum at 60 °C for 4 h. The metal cations ratios of Ni^{2+} to Fe^{3+} were maintained at a 3:1 ratio, with total metal cations of 0.5 mmol, 1.0 mmol, and 2.0 mmol, respectively. The samples were labeled as 0.5-LDH/MXNF, 1.0-LDH/MXNF, and 2.0-LDH/MXNF, respectively.

Additionally, two comparative samples, 1.0-LDH/NF and 1.0-LDH/3MCNF, were prepared under identical conditions. The 3MCNF in the 1.0-LDH/3MCNF sample represents NF treated with 3 mg/mL of f-$Ti_3C_2T_x$.

3.4. Structural Characterization

The crystal phase of the catalyst was analyzed using an X-ray diffractometer (XRD, ADVANCE D8, Bruker, Billerica, MA, USA) with a Cu Kα radiation source in the range of 2θ of 5°~80°. The chemical composition of the catalyst was investigated using Fourier transform infrared spectroscopy with attenuated total reflection (FTIR-ATR, Thermo Scientific, Nicolet iS50, Waltham, MA, USA). The morphology of the obtained catalyst was characterized by a thermal field emission scanning electron microscope (SEM, Zeiss Gemini Sigma 300, Goldbach, Germany) equipped with energy-dispersive spectroscopy (EDS). Transmission electron microscopy (TEM, Talos F200X, Thermo Fisher Scientific, Waltham, MA, USA) was used to identify the catalyst's morphology and elemental mapping. X-ray photoelectron spectra (XPS) were recorded in an XPS system (Axis Ultra DLD, Kratos, Manchester, UK) with a monochromatic Al X-ray source.

3.5. Electrochemical Measurements

All electrochemical properties were assessed in a standard three-electrode system using a Shanghai Chenhua CHI 760E electrochemical workstation. A mercuric oxide electrode (Hg/HgO) was used as the reference electrode, a graphite rod as the counter electrode, and the as-prepared catalyst as the working electrode. The two-sided geometry of the self-supported electrode was 1.2 cm^2, with a catalyst mass loading of 0.5 mg/cm^2. The electrochemical performance of the catalyst was evaluated in 1 M KOH solution. All measured potentials were converted to reversible hydrogen potential (RHE) based on the Hg/HgO calibration potential and the Nernst equation. The prepared catalysts underwent linear sweep voltammetry (LSV) tests to evaluate their OER activity at a sweep rate of 5 mV/s after 30 cycles of cyclic voltammetry (CV) activation in an O_2-saturated 1.0 M

KOH electrolyte. A 90% iR compensation was applied to all potentials in the LSV curve. CV measurements were carried out in the non-Faradaic zone at various sweep rates of 20, 40, 60, 80, 100, and 120 mV/s to evaluate the electrochemical double layer capacitance (C_{dl}) of the electrocatalysts. Electrochemical impedance spectroscopy (EIS) measurements were performed at 1.53 V vs. RHE using a 5 mV amplitude over a frequency range of 10^5 to 0.1 Hz. Multi-step chronopotentiometric curves were obtained by altering the current densities from 50 to 200 mA cm^{-2} with an increment of 50 mA cm^{-2} per 300 s before finally returning to 50 mA cm^{-2} for an extended period. Chronopotentiometry (CP) curves were recorded as the current densities reached 50 mA cm^{-2} to evaluate catalyst stability.

The Tafel slopes were calculated using the following formula:

$$\eta = b\ log\ j + c \tag{1}$$

where η is the overpotential, j is the current density, b is the Tafel slope, and c is the intercept.

The Electrochemical Active Surface Area (ECSA) of the electrocatalysts was estimated from C_{dl} according to the following formula [61]:

$$ECSA = C_{dl}/C_s \tag{2}$$

where the specific capacitance (C_s) is 40 mF/cm^2.

4. Conclusions

In conclusion, the foam nickel loaded with Ti_3CNT_x MXene-modified NiFe-LDH, developed through electrostatic adsorption and hydrothermal methods, exhibits excellent electrocatalytic performance for the oxygen evolution reaction. By adjusting the thickness of NiFe-LDH nanosheets and the MXene content, the OER performance of the self-standing electrode can be altered. In addition, the vertical structure of the LDH nanosheets facilitates mass transfer during the catalytic process. The 1.0-LDH/3MXNF catalyst showcased a low overpotential of 247 mV at 100 mA cm^{-2} and a Tafel slope of 67.7 mV/dec, attributed to the effective interfacial coupling between NiFe-LDH and MXene, which enhanced electron transfer kinetics. The electrochemical characterization revealed a significant increase in electrochemical double-layer capacitance and a reduction in charge transfer resistance, indicating a high density of active sites and efficient charge transport. Additionally, the electrode exhibited remarkable stability with minimal potential degradation over long-term operation. This study highlights the promising potential of hybrid LDH-MXene systems for advanced electrocatalyst development in renewable energy applications.

Supplementary Materials: The following supporting information can be downloaded at: https://www.mdpi.com/article/10.3390/catal14100708/s1, Figure S1: SEM image of (a) Ti_3AlCN and (b) m-Ti_3CNT_x; Figure S2: XRD patterns of Ti_3AlCN MAX and Ti_3CNT_x MXene; Figure S3: (a) XRD patterns and (b) ART-FTIR spectrum of LDH/5MXNF; Figure S4: SEM image of (a) NF, (b) 3MXNF, and (c) 5MXNF; Figure S5: SEM image of elemental mapping showing the uniform distribution of Ti, N, Ni, and Fe elements in 1-LDH/3MXNF; Figure S6: SEM image of (a) 0.5-LDH/3MXNF, (b) 1.0-LDH/3MXNF, and (c) 2.0-LDH/3MXNF; Figure S7: SEM image of (a) 0.5-LDH/5MXNF, (b) 1.0-LDH/5MXNF, and (c) 2.0-LDH/5MXNF; Figure S8: Full spectrum of (a) 1.0-LDH/NF and (b) 1.0-LDH/3MXNF; Figure S9: The calibration curve of Hg/HgO electrode vs. RHE. The calibration was performed in a high-purity hydrogen-saturated electrolyte with Pt sheet as the working electrode and Hg/HgO electrode as the reference electrode. CV runs at a scan rate of 1 mV/s, and the average of the two potentials at the current zero crossing is considered to be the thermodynamic potential of the hydrogen electrode reaction. In the 1.0 M KOH, E (vs. RHE) = E (vs. Hg/HgO) + 0.92 V; Figure S10: OER CV curves for (a) pure NF; (b) 1.0-LDH/NF; (c) 1.0-LDH/3MCNF; (d) 0.5-LDH/3MXNF; (e) 1.0-LDH/3MXNF; (f) 2.0-LDH/3MXNF; (g) 0.5-LDH/5MXNF; (h) 1.0-LDH/5MXNF; and (i) 2-LDH/5MXNF; Figure S11: The OER performance of the LDH/5MXNF in 1.0 M KOH. (a) LSV curves; (b) Tafel plots; (c) the C_{dl}; and (d) EIS patterns at 1.53 V vs. RHE; Figure S12: (a) LSV curves of LDH/Ti_3CN, NiFe-LDH, and Ti_3CN powder loaded on glass carbon electrode for OER. (b) EIS curves of LDH/Ti_3CN and NiFe-LDH power at 1.53 V vs. RHE from 10^5 to 0.1 Hz. (c) Tafel slope.

(d) Double-layer capacitance C_{dl}. (e,f) Corresponding CV of NiFe-LDH and LDH/Ti_3CN. All LSV tests were conducted at a scan rate of 5 mV s^{-1} at 1600 rpm with 90% iR-compensations. The mass loading is about 0.214 mg cm^{-2}. All tests were conducted in 1 M KOH.

Author Contributions: Conceptualization, L.H., Q.T., Q.F. and H.Z.; formal analysis, L.H., H.Z. and Y.P.; funding acquisition, K.L.; investigation, Q.T., Q.F., Y.P. and S.W.; methodology, Q.T., S.W. and K.L.; supervision, K.L.; writing—original draft, L.H.; writing—review and editing, K.L. All authors have read and agreed to the published version of the manuscript.

Funding: This study was financially supported by National Natural Science Foundation of China (Grant No. U23A2093 and 12375279), High-Level Talents Special Support Program of Zhejiang Province (2022R51007), Ningbo Top-talent Team Program, and Youth Science and Technology Innovation Leading Talent Project of Ningbo. KL gratefully acknowledges financial support from Anglo American Resources Trading (China) Co., Ltd.

Data Availability Statement: Data are contained within the article.

Conflicts of Interest: The authors declare no conflicts of interests.

References

1. De Luna, P.; Hahn, C.; Higgins, D.; Jaffer, S.A.; Jaramillo, T.F.; Sargent, E.H. What would it take for renewably powered electrosynthesis to displace petrochemical processes? *Science* **2019**, *364*, 6438. [CrossRef] [PubMed]
2. Yan, L.; Du, Z.; Lai, X.; Lan, J.; Liu, X.; Liao, J.; Feng, Y.; Li, H. Synergistically modulating the electronic structure of Cr-doped FeNi LDH nanoarrays by O-vacancy and coupling of MXene for enhanced oxygen evolution reaction. *Int. J. Hydrogen Energy* **2023**, *48*, 1892–1903. [CrossRef]
3. Sun, L.; Reddu, V.; Fisher, A.C.; Wang, X. Electrocatalytic reduction of carbon dioxide: Opportunities with heterogeneous molecular catalysts. *Energy Environ. Sci.* **2020**, *13*, 374–403. [CrossRef]
4. Chen, M.; Fan, Q.; Chen, K.; Majkova, E.; Huang, Q.; Liang, K. MXene materials: Pioneering sustainable energy storage solutions. *Carbon Neutralization* **2024**, *3*, 493–500. [CrossRef]
5. Gür, T.M. Review of electrical energy storage technologies, materials and systems: Challenges and prospects for large-scale grid storage. *Energy Environ. Sci.* **2018**, *11*, 2696–2767. [CrossRef]
6. Zeng, F.; Mebrahtu, C.; Liao, L.; Beine, A.K.; Palkovits, R. Stability and deactivation of OER electrocatalysts: A review. *J. Energy Chem.* **2022**, *69*, 301–329. [CrossRef]
7. Trasatti, S. Electrocatalysis by oxides—Attempt at a unifying approach. *J. Electroanal. Chem. Interfacial Electrochem.* **1980**, *111*, 125–131. [CrossRef]
8. Walter, M.G.; Warren, E.L.; McKone, J.R.; Boettcher, S.W.; Mi, Q.; Santori, E.A.; Lewis, N.S. Solar Water Splitting Cells. *Chem. Rev.* **2010**, *110*, 6446–6473. [CrossRef]
9. Luo, J.; Matios, E.; Wang, H.; Tao, X.; Li, W. Interfacial structure design of MXene-based nanomaterials for electrochemical energy storage and conversion. *InfoMat* **2020**, *2*, 1057–1076. [CrossRef]
10. Khateri, M.; Najafpour, M.M. Oxygen-Evolution Reaction on Nickel Oxyhydroxide's Surface: Toward a Super Catalyst for Oxygen-Evolution Reaction with Ultralow Overpotentials. *ACS Appl. Energy Mater.* **2024**, *7*, 5028–5037. [CrossRef]
11. Liu, S.; Wang, F.; Wang, J.; Wang, Z.; He, X.; Zhang, T.; Zhang, Z.; Liu, Q.; Liu, X.; Zhang, X. Dense heterogeneous interfaces boost the electrocatalytic oxygen evolution reaction. *Appl. Catal. B Environ. Energy* **2024**, *355*, 124148. [CrossRef]
12. Gebauer, C.; Fischer, P.; Wassner, M.; Diemant, T.; Jusys, Z.; Hüsing, N.; Behm, R.J. Performance of titanium oxynitrides in the electrocatalytic oxygen evolution reaction. *Nano Energy* **2016**, *29*, 136–148. [CrossRef]
13. Jiang, T.; Xie, W.; Geng, S.; Li, R.; Song, S.; Wang, Y. Constructing oxygen vacancy-regulated cobalt molybdate nanoflakes for efficient oxygen evolution reaction catalysis. *Chin. J. Catal.* **2022**, *43*, 2434–2442. [CrossRef]
14. Anne, B.R.; Kundu, J.; Kabiraz, M.K.; Kim, J.; Cho, D.; Choi, S.-I. A Review on MXene as Promising Support Materials for Oxygen Evolution Reaction Catalysts. *Adv. Funct. Mater.* **2023**, *33*, 2306100. [CrossRef]
15. Chen, X.; Xu, X.; Shao, C.; Ke, Z.; Cheng, Y.; Jin, H.; Da, Y.; Liu, D.; Chen, W. Facet-Dependent Lattice Oxygen Activation on Oxygen-Defective Co_3O_4 for Electrocatalytic Oxygen Evolution Reaction. *ACS Energy Lett.* **2024**, *9*, 2182–2192. [CrossRef]
16. Liao, Y.; He, R.; Pan, W.; Li, Y.; Wang, Y.; Li, J.; Li, Y. Lattice distortion induced Ce-doped NiFe-LDH for efficient oxygen evolution. *Chem. Eng. J.* **2023**, *464*, 142669. [CrossRef]
17. Lei, L.; Huang, D.; Zhou, C.; Chen, S.; Yan, X.; Li, Z.; Wang, W. Demystifying the active roles of NiFe-based oxides/(oxy)hydroxides for electrochemical water splitting under alkaline conditions. *Coord. Chem. Rev.* **2020**, *408*, 213177. [CrossRef]
18. Xu, X.; Zhong, Y.; Wajrak, M.; Bhatelia, T.; Jiang, S.P.; Shao, Z. Grain boundary engineering: An emerging pathway toward efficient electrocatalysis. *InfoMat* **2024**, *6*, e12608. [CrossRef]
19. Jin, Z.; Liu, C.; Liu, Z.; Han, J.; Fang, Y.; Han, Y.; Niu, Y.; Wu, Y.; Sun, C.; Xu, Y. Rational Design of Hydroxyl-Rich $Ti_3C_2T_x$ MXene Quantum Dots for High-Performance Electrochemical N_2 Reduction. *Adv. Energy Mater.* **2020**, *10*, 2000797. [CrossRef]
20. Kan, D.; Wang, D.; Zhang, X.; Lian, R.; Xu, J.; Chen, G.; Wei, Y. Rational design of bifunctional ORR/OER catalysts based on Pt/Pd-doped Nb_2CT_2 MXene by first-principles calculations. *J. Mater. Chem. A* **2020**, *8*, 3097–3108. [CrossRef]

21. Li, T.; Yan, X.; Huang, L.; Li, J.; Yao, L.; Zhu, Q.; Wang, W.; Abbas, W.; Naz, R.; Gu, J.; et al. Fluorine-free $Ti_3C_2T_x$ (T = O, OH) nanosheets (∼50–100 nm) for nitrogen fixation under ambient conditions. *J. Mater. Chem. A* **2019**, *7*, 14462–14465. [CrossRef]
22. Xiu, L.; Wang, Z.; Yu, M.; Wu, X.; Qiu, J. Aggregation-Resistant 3D MXene-Based Architecture as Efficient Bifunctional Electrocatalyst for Overall Water Splitting. *ACS Nano* **2018**, *128*, 8017–8028. [CrossRef] [PubMed]
23. Zhao, M.-Q.; Xie, X.; Ren, C.E.; Makaryan, T.; Anasori, B.; Wang, G.; Gogotsi, Y. Hollow MXene Spheres and 3D Macroporous MXene Frameworks for Na-Ion Storage. *Adv. Mater.* **2017**, *29*, 1702410. [CrossRef] [PubMed]
24. Zhang, C.; Cui, L.; Abdolhosseinzadeh, S.; Heier, J. Two-dimensional MXenes for lithium-sulfur batteries. *InfoMat* **2020**, *2*, 613–638. [CrossRef]
25. Li, M.; Fan, Q.; Gao, L.; Liang, K.; Huang, Q. Chemical Intercalation of Layered Materials: From Structure Tailoring to Applications. *Adv. Mater.* **2024**, *36*, 2312918. [CrossRef]
26. Liang, K.; Tabassum, A.; Majed, A.; Dun, C.; Yang, F.; Guo, J.; Prenger, K.; Urban, J.J.; Naguib, M. Synthesis of new two-dimensional titanium carbonitride $TiC_{0.5}N_{0.5}T_x$ MXene and its performance as an electrode material for sodium-ion battery. *InfoMat* **2021**, *3*, 1422–1430. [CrossRef]
27. Zong, H.; Hu, L.; Gong, S.; Yu, K.; Zhu, Z. Flower-petal-like Nb2C MXene combined with MoS2 as bifunctional catalysts towards enhanced lithium-sulfur batteries and hydrogen evolution. *Electrochim. Acta* **2022**, *404*, 139781. [CrossRef]
28. Zhou, A.; Liu, Y.; Li, S.; Wang, X.; Ying, G.; Xia, Q.; Zhang, P. From structural ceramics to 2D materials with multi-applications: A review on the development from MAX phases to MXenes. *J. Adv. Ceram.* **2021**, *10*, 1194–1242. [CrossRef]
29. Jin, S.; Guo, Y.; Wang, F.; Zhou, A. The synthesis of MXenes. *MRS Bull.* **2023**, *48*, 245–252. [CrossRef]
30. Ding, H.; Li, Y.; Li, M.; Chen, K.; Liang, K.; Chen, G.; Lu, J.; Palisaitis, J.; Persson, P.O.Å.; Eklund, P.; et al. Chemical scissor–mediated structural editing of layered transition metal carbides. *Science* **2023**, *379*, 1130–1135. [CrossRef]
31. Liang, K.; Wu, T.; Misra, S.; Dun, C.; Husmann, S.; Prenger, K.; Urban, J.J.; Presser, V.; Unocic, R.R.; Jiang, D.-E.; et al. Nitrogen-Doped Graphene-Like Carbon Intercalated MXene Heterostructure Electrodes for Enhanced Sodium- and Lithium-Ion Storage. *Adv. Sci.* **2024**, *11*, 2402708. [CrossRef] [PubMed]
32. Kan, D.; Lian, R.; Wang, D.; Zhang, X.; Xu, J.; Gao, X.; Yu, Y.; Chen, G.; Wei, Y. Screening effective single-atom ORR and OER electrocatalysts from Pt decorated MXenes by first-principles calculations. *J. Mater. Chem. A* **2020**, *8*, 17065–17077. [CrossRef]
33. Shi, Y.; Liu, Y. Vacancy and N dopants facilitated Ti^{3+} sites activity in 3D $Ti_{3-x}C_2T_y$ MXene for electrochemical nitrogen fixation. *Appl. Catal. B Environ.* **2021**, *297*, 120482. [CrossRef]
34. Yang, Z.; Yang, Q.; Tian, Y.; Ren, X.; Li, C.; Zu, Y.; Din, S.Z.U.; Gao, L.; Wu, J.; Chen, H.; et al. Few-layer Ti_3CN MXene for ultrafast photonics applications in visible band. *J. Mater.* **2023**, *9*, 44–55. [CrossRef]
35. Guo, W.; She, Z.; Xue, H.; Zhang, X. Density functional theory study on the Ti_3CN and Ti_3CNT_2 (T = O, S and F) as high capacity anode material for Na ion batteries. *Appl. Surf. Sci.* **2020**, *529*, 147180. [CrossRef]
36. Cao, S.; Huang, H.; Shi, K.; Wei, L.; You, N.; Fan, X.; Yang, Z.; Zhang, W. Engineering superhydrophilic/superaerophobic hierarchical structures of Co-CH@NiFe-LDH/NF to boost the oxygen evolution reaction. *Chem. Eng. J.* **2021**, *422*, 130123. [CrossRef]
37. Zheng, Z.; Wu, D.; Chen, G.; Zhang, N.; Wan, H.; Liu, X.; Ma, R. Microcrystallization and lattice contraction of NiFe LDHs for enhancing water electrocatalytic oxidation. *Carbon Energy* **2022**, *4*, 901–913. [CrossRef]
38. Gu, Y.; Park, D.-H.; Kim, M.-H.; Byeon, J.-H.; Lim, D.-M.; Park, S.-H.; Kim, J.-H.; Jang, J.-S.; Park, K.-W. NiFe layered double hydroxides synthesized based on solvent properties as anode catalysts for enhanced oxygen evolution reaction. *Chem. Eng. J.* **2024**, *480*, 147789. [CrossRef]
39. Ko, Y.-J.; Han, M.H.; Kim, H.; Kim, J.-Y.; Lee, W.; Kim, J.; Kwak, J.Y.; Kim, C.-H.; Park, T.-E.; Yu, S.-H.; et al. Unraveling Ni-Fe 2D nanostructure with enhanced oxygen evolution via in situ and operando spectroscopies. *Chem Catal.* **2022**, *2*, 2312–2327. [CrossRef]
40. Xiang, Y.; He, Y.; Zhang, W.; Li, B.; Li, H.; Wang, Y.; Yin, X.; Tang, W.; Li, Z.; He, Z. Superhydrophobic LDH/TTOS composite surface based on microstructure for the anti-corrosion, anti-fouling and oil-water separation application. *Colloids Surf. A Physicochem. Eng. Asp.* **2021**, *622*, 126558. [CrossRef]
41. Chenakin, S.; Kruse, N. XPS characterization of transition metal oxalates. *Appl. Surf. Sci.* **2020**, *515*, 146041. [CrossRef]
42. Kong, Y.; Wang, Y.; Chu, W.; Liu, Z. Tailoring surface and interface electronic structure of NiFe LDH via V doping for enhanced oxygen evolution reaction. *J. Alloys Compd.* **2021**, *885*, 160929. [CrossRef]
43. Huang, K.; Dong, R.; Wang, C.; Li, W.; Sun, H.; Geng, B. Fe–Ni Layered Double Hydroxide Arrays with Homogeneous Heterostructure as Efficient Electrocatalysts for Overall Water Splitting. *ACS Sustain. Chem. Eng.* **2019**, *7*, 15073–15079. [CrossRef]
44. Li, X.-P.; Han, W.-K.; Xiao, K.; Ouyang, T.; Li, N.; Peng, F.; Liu, Z.-Q. Enhancing hydrogen evolution reaction through modulating electronic structure of self-supported NiFe LDH. *Catal. Sci. Technol.* **2020**, *10*, 4184–4190. [CrossRef]
45. Hao, N.; Wei, Y.; Wang, J.; Wang, Z.; Zhu, Z.; Zhao, S.; Han, M.; Huang, X. In situ hybridization of an MXene/TiO_2/NiFeCo-layered double hydroxide composite for electrochemical and photoelectrochemical oxygen evolution. *RSC Adv.* **2018**, *8*, 20576–20584. [CrossRef]
46. Hu, L.; Li, M.; Wei, X.; Wang, H.; Wu, Y.; Wen, J.; Gu, W.; Zhu, C. Modulating interfacial electronic structure of CoNi LDH nanosheets with $Ti_3C_2T_x$ MXene for enhancing water oxidation catalysis. *Chem. Eng. J.* **2020**, *398*, 125605. [CrossRef]
47. Yang, Z.; Lin, Y.; Jiao, F.; Li, J.; Wang, J.; Gong, Y. In situ growth of 3D walnut-like nano-architecture Mo-Ni_2P@NiFe LDH/NF arrays for synergistically enhanced overall water splitting. *J. Energy Chem.* **2020**, *49*, 189–197. [CrossRef]

48. Su, C.; Wang, D.; Wang, W.; Mitsuzaki, N.; Shao, R.; Xu, Q.; Chen, Z. Rational design of bimetallic metal-organic framework derived three-dimensional flower-like and porous NiCoFe LDH/NF electrocatalyst for electrochemical overall water splitting. *J. Electroanal. Chem.* **2024**, *960*, 118167. [CrossRef]
49. Hu, Y.; Wang, Z.; Liu, W.; Xu, L.; Guan, M.; Huang, Y.; Zhao, Y.; Bao, J.; Li, H.-M. Novel Cobalt–Iron–Vanadium Layered Double Hydroxide Nanosheet Arrays for Superior Water Oxidation Performance. *ACS Sustain. Chem. Eng.* **2019**, *7*, 16828–16834. [CrossRef]
50. Gupta, A.; Sadhanala, H.K.; Gedanken, A. Iron doped cobalt nickel layered double hydroxide supported on nickel foam as a robust electrocatalyst for highly efficient water oxidation in alkaline sea water. *Electrochim. Acta* **2023**, *470*, 143269. [CrossRef]
51. Ullah, S.; Ahmed, W.; Zeeshan, M.; Hu, S.; Zhang, X. Integral 2D/3D structured $CoSnO_3$@MXene/NF as a highly active and stable bifunctional electrocatalyst for alkaline water splitting. *Int. J. Hydrogen Energy* **2024**, *70*, 448–460. [CrossRef]
52. Guo, Y.; Wang, P.; Li, P.; Tang, M.; Yin, H.; Wang, D. A highly efficient and durable self-standing iron-cobalt-nickel trimetallic phosphide electrode for oxygen evolution reaction. *J. Alloys Compd.* **2023**, *960*, 170493. [CrossRef]
53. Li, L.; Wang, Z.; She, X.; Pan, L.; Xi, C.; Wang, D.; Yi, J.; Yang, J. Ni-modified FeOOH integrated electrode by self-source corrosion of nickel foam for high-efficiency electrochemical water oxidation. *J. Colloid Interface Sci.* **2023**, *652*, 789–797. [CrossRef] [PubMed]
54. Jeong, M.; Park, S.; Kwon, T.; Kwon, M.; Yuk, S.; Kim, S.; Yeon, C.; Lee, C.-W.; Lee, D. Interface Engineering via $Ti_3C_2T_x$ MXene Enabled Highly Efficient Bifunctional NiCoP Array Catalysts for Alkaline Water Splitting. *ACS Appl. Mater. Interfaces* **2024**, *16*, 34798–34808.
55. Chen, J.; Liu, C.; Ren, W.; Sun, J.; Zhang, Y.; Zou, L. Synergistic effect of NF and rGO in preparing 3D NiFe-LDH/rGO@NF composites on electrocatalysts performance. *J. Alloys Compd.* **2022**, *901*, 163510. [CrossRef]
56. Shen, B.; Feng, Y.; Wang, Y.; Sun, P.; Yang, L.; Jiang, Q.; He, H.; Huang, H. Holey MXene nanosheets intimately coupled with ultrathin Ni–Fe layered double hydroxides for boosted hydrogen and oxygen evolution reactions. *Carbon* **2023**, *212*, 118141. [CrossRef]
57. Wang, X.; Wang, N.; Zhou, X.; Yue, Z.; Shan, Y.; Chen, K.; Yu, X. MXene introduced between CoNi LDH and NiMoO4 nanorods arrays: A bifunctional multistage composite for OER catalyst and supercapacitors. *Int. J. Hydrogen Energy* **2024**, *86*, 719–729. [CrossRef]
58. Zuo, W.; Lan, X.; Lv, G.; Yang, C.; Lan, P.; Peng, B.; Liu, P.; Li, K. Sulfur and Phosphorus Co-Doped CoFeLDH/MXene Nanoarray Electrocatalyst for the Oxygen Evolution Reaction. *ACS Appl. Nano Mater.* **2024**, *7*, 11599–11608. [CrossRef]
59. Sun, Y.; Wang, Z.; Zhou, Q.; Li, X.; Zhao, D.; Ding, B.; Wang, S. Ti_3C_2 mediates the NiFe-LDH layered electrocatalyst to enhance the OER performance for water splitting. *Heliyon* **2024**, *10*, e30966. [CrossRef]
60. Liang, K.; Tabassum, A.; Kothakonda, M.; Zhang, X.; Zhang, R.; Kenney, B.; Koplitz, B.D.; Sun, J.; Naguib, M. Two-dimensional titanium carbonitride MXene as a highly efficient electrocatalyst for hydrogen evolution reaction. *Mater. Rep. Energy* **2022**, *2*, 100075. [CrossRef]
61. Liang, K.; Guo, L.; Marcus, K.; Zhang, S.; Yang, Z.; Perea, D.E.; Zhou, L.; Du, Y.; Yang, Y. Overall Water Splitting with Room-Temperature Synthesized NiFe Oxyfluoride Nanoporous Films. *ACS Catal.* **2017**, *7*, 8406–8412. [CrossRef]